PROCEEDINGS, 42nd Workshop on Geothermal Reservoir Engineering
Stanford University, Stanford, California, February 13-15, 2017
SGP-TR-212

Towards a Better Understanding of the Impact of Fracture Roughness on Permeability-Stress Relationships using First Principles

Carla Co[1*], David Pollard[2], and Roland Horne[1]

[1]Department of Energy Resources Engineering, Stanford University, Stanford, CA 94305

[2]Department of Geological Sciences, Stanford University, Stanford, CA 94305

[*]carlakdc@stanford.edu

Keywords: boundary element method, fracture aperture, permeability-stress relationships

ABSTRACT

For conventional and enhanced geothermal reservoirs, faults and fractures are the main conduits for flow. In geomechanical simulations, empirical models are typically used to calculate the changes in fracture permeability due to stress application. However, determining the appropriate model parameters is often problematic due to the lack of available data and the difficulty of performing shear experiments. The displacement discontinuity boundary element method with integrated complementarity (DDM) is an advantageous alternative approach because it is a consistent physical model that simulates fracture permeability evolution under changing stress conditions.

In this study, the DDM model was used to investigate the changes in permeability due to applied stress conditions for rough fractures. Fracture aperture maps for the different stress conditions were generated using the DDM model. Afterwards, a local cubic law model was used to calculate the fracture permeability. Results showed that the roughness of the fracture surface created stress interactions that led to local opening in the absence of a fluid within the fracture. The rough fracture surface also created heterogeneous fracture aperture and slip distributions. Overall, the fracture permeability and average slip increased with the shear stress magnitude and decreased with the normal stress magnitude. Moreover, it was demonstrated that the fracture permeability was higher in the direction perpendicular to the applied shear stress direction compared to the parallel direction.

1. INTRODUCTION

Accurate modeling of fracture flow behavior is important for tight reservoirs, such as shale gas and geothermal systems, where faults and fractures are the main conduits for flow. In enhanced geothermal systems (EGS), hydraulic fracturing is used to increase permeability by creating new fractures or inducing slip on preexisting fractures (McClure and Horne, 2011). If appropriate investments in research and development are made, EGS has a potential of having up to 100 GWe of generating capacity in the next 50 years (Tester et al., 2006). Considering the great potential for EGS, a fundamental understanding of the physics of fracture deformation and flow are necessary for optimizing geothermal energy production.

Typically, it is assumed that faults and fractures have smooth surfaces with constant aperture and permeability values. However, field data have shown that real faults and fractures have rough surfaces that can modify fluid flow pathways significantly (Ritz et al., 2012). Moreover, flow experiments conducted on rough-walled fractures have demonstrated channeling flow behavior, where only 30 percent of the fracture area was conducive to flow (Ishibashi et al., 2012). Flow channeling also reduces the cross-sectional area available for heat conduction, which can lead to inadequate heating of injected fluids in the reservoir.

The spatial distribution of aperture and permeability values within the fracture plane can be modified by the application of stress. Numerous experiments have demonstrated the evolution of fracture aperture and permeability due to applied normal and shear stresses (Barton et al., 1985; Esaki et al., 1999; Lee and Cho, 2002; Gutierrez et al., 2000). However, due to limitations in equipment capabilities and configurations, local normal and shear displacement values cannot be measured. Moreover, inelastic deformation and local stress concentrations constantly alter the local surface roughness, making it difficult to isolate the impact of fracture roughness. Inelastic effects such as gouge formation and rock breakage change the fracture permeability. Thus, it is hard to develop a fundamental understanding of the impact of roughness due to the complexity of the interacting mechanisms in the model.

Several empirical models have likewise been developed to quantify the impact of applied stress conditions on the fracture permeability (Barton et al., 1985; Willis-Richards et al., 1996; Dempsey et al., 2013). These empirical models are used commonly in geomechanical simulation models (McClure and Horne, 2011). Though these empirical models are useful for general estimations of changes in permeability with stress, it is very difficult to determine the appropriate values for model constants that are applicable for a specific system under a wide range of stress conditions. Furthermore, performing the necessary experiments to determine the correct constants requires significant effort.

Because of the limitations of empirical equations and laboratory experiments, a consistent physical model is needed for the accurate modeling of fracture permeability evolution with stress. Thus, the displacement discontinuity boundary element method with integrated complementarity (DDM) is a viable alternative. In this study, the main objective was to investigate the impact of fracture surface

roughness on permeability-stress relationships using the DDM model. Furthermore, the changes in the spatial distribution of the fracture aperture and flow pathways due to stress application were also analyzed.

2. DDM WITH INTEGRATED COMPLEMENTARITY

The displacement discontinuity boundary element method with integrated complementarity (DDM) simulates the normal and shear displacements from imposed stress conditions (Ritz et al., 2012). Assuming elastic behavior, the DDM model can handle rough fracture surfaces by accounting for stress interactions among elements within the fracture. Moreover, the integrated complementarity algorithm improves the original DDM model by ensuring consistent contact boundary conditions and preventing nonphysical surface overlapping. Additionally, the DDM model utilizes standard elastic properties from core characterization tests. Figure 1 illustrates the general features of the DDM model. The total fracture trace is subdivided into smaller elements. To describe the frictional sliding at each element, the Coulomb criterion is used as shown in Equation 1:

$$\sigma_{ns} \leq -\mu\sigma_{nn} + S_f, \quad \sigma_{nn} \leq 0 \tag{1}$$

where, σ_{ns} is the magnitude of the shear traction vector, μ is the coefficient of friction, σ_{nn} is the magnitude of the normal traction vector, and S_f is the frictional strength.

The values for μ range from 0.5 to 0.8 with 0.6 as the typical value (Pollard and Fletcher, 2005). For prefractured rocks, the S_f value is negligible up to depths of approximately 8 km (Ritz et al., 2012). Under the DDM formulation shown in Equation 2, the normal displacement or opening (D_n) and shear displacement or slip (D_s) for each element (i) are related to the normal (σ_{nn}) and shear (σ_{ns}) stresses of all the elements in the fracture (j) by the inverse of the original influence coefficients $(C_{nn}, C_{ns}, C_{sn}, C_{ss})$. Expressions for $(C_{nn}, C_{ns}, C_{sn}, C_{ss})$ can be found in Crouch and Starfield (1983). Finally, defining inequality pairs in a complementarity formulation enforces contact boundary conditions and prevents overlapping between the two fracture walls (Ritz et al., 2012).

$$\begin{aligned} [D_n]_i &= [C_{nn}]_{ij}[\sigma_{nn}]_j + [C_{ns}]_{ij}[\sigma_{ns}]_j \\ [D_s]_i &= [C_{sn}]_{ij}[\sigma_{nn}]_j + [C_{ss}]_{ij}[\sigma_{ns}]_j \end{aligned} \tag{2}$$

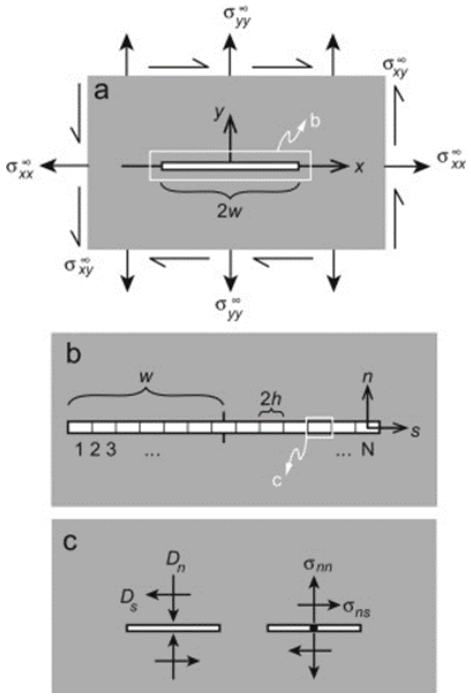

Figure 1: The displacement discontinuity boundary element method (DDM). (a) Infinite two-dimensional plane with an embedded crack of length $2w$. σ_{xx}^{∞}, σ_{yy}^{∞}, and σ_{xy}^{∞} are the applied remote stresses. The positive stress sign convention is shown here. (b) Discretization of the crack surface into N elements, each with length equal to $2h$. The normal (n) and shear (s) directions are shown here. (c) The positive sign convention for the displacement discontinuities and stress components. The displacement discontinuities are opening (D_n) and slip (D_s) while the stress components are normal (σ_{nn}) and shear (σ_{ns}) (from Ritz et al., 2012)

3. METHODOLOGY

Fracture surfaces elevation maps were obtained from granite and sandstone core samples sheared in compression tests performed by David Lockner at the United States Geological Survey in Menlo Park, CA. Afterwards, Rebecca Strickfaden measured surface elevation values using a laser scanner with a measurement accuracy of $\pm 0.1270\ mm$. Assuming full initial contact of the two sides of the fracture, two-dimensional DDM models were simulated for individual fracture traces within the fracture plane. Remote stresses with $\sigma_{xx}^r, \sigma_{yy}^r$, and σ_{xy}^r components were applied with $\sigma_{xx}^r = \sigma_{yy}^r$. For simplicity, $\sigma_{nn}^r = \sigma_{xx}^r = \sigma_{yy}^r$ and $\sigma_{ns}^r = \sigma_{xy}^r$ are defined as the applied remote normal and shear stresses, respectively. Individual fracture DDM results were combined to generate the results for the whole fracture plane. This DDM modeling approach accounts for the relevant stress interactions among the elements within the fracture trace and along the direction of shear. Stress interactions among fracture traces within the fracture plane are less significant because they are in the direction perpendicular to shear. Fracture traces were obtained from the surface elevation maps in the X and Y directions. Figure 2a shows a sample fracture trace along the Y axis (constant X value) that was used in the DDM model. Convergence studies were performed to ensure that the DDM results were accurate. Preprocessing of the fracture traces was needed to achieve converged DDM results. Fourier filtering was applied to eliminate sharp corners, which create instabilities in the DDM calculations. A two-dimensional, second order Butterworth low-pass filter (Roberts and Roberts, 1978) was applied to keep some high frequency information and retain the essential elements of the original fracture shape.

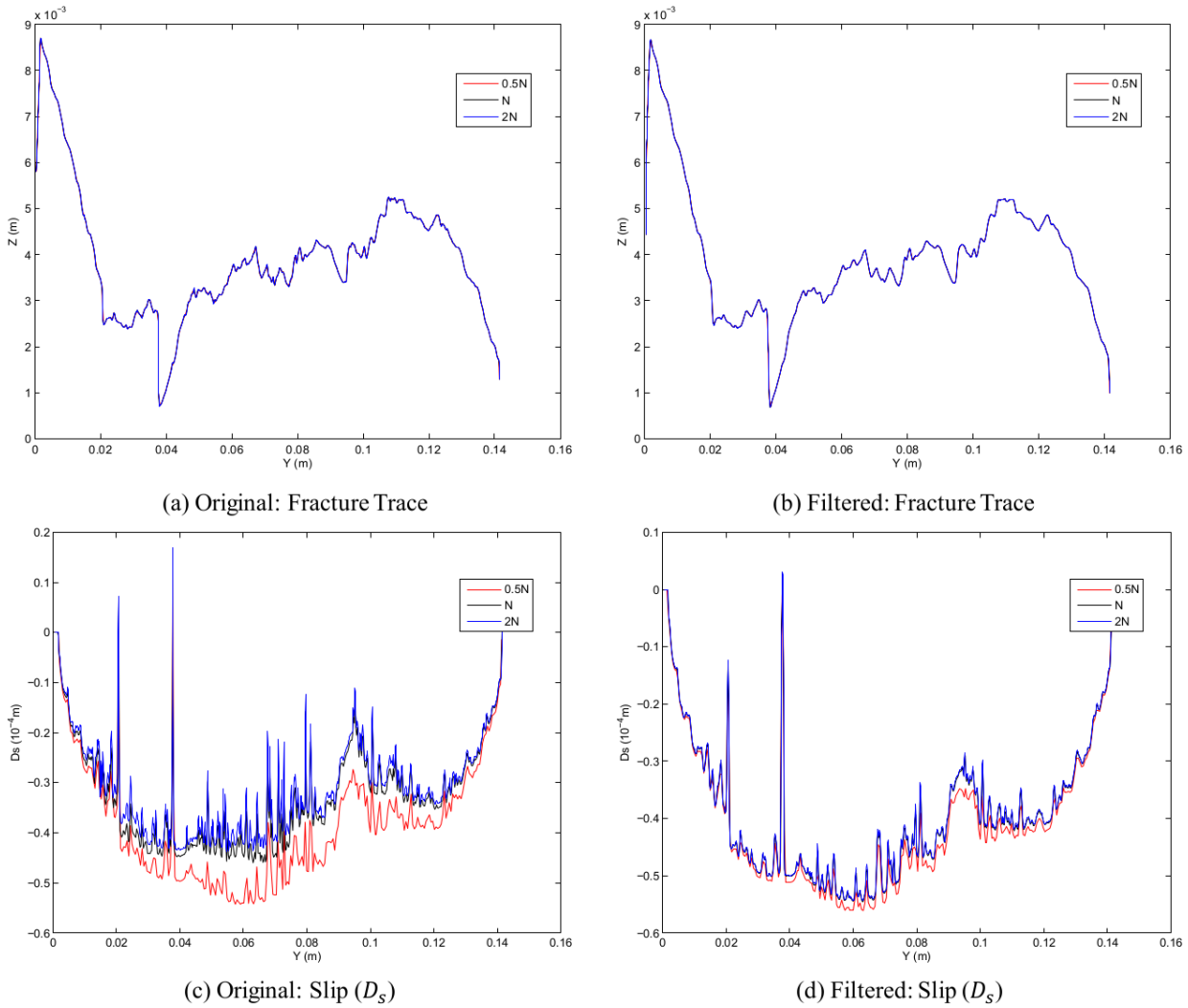

Figure 2: Convergence comparison for the original and filtered (Butterworth low pass filter with $w_o = 0.40\ w_{max}$) fractures. N is the original number of elements for the fracture trace, Z is the elevation value, and Y is the longitudinal axis in the original fracture plane. The application of the Butterworth filter resulted to a converged DDM result.

Equation 3 shows the expression for the two-dimensional frequency (w), where u and v are frequency values in the X and Y directions. The expression for the applied low-pass Butterworth filter (H) is shown in Equation 4, where w_o is the cut-off frequency. For simplicity, w_o can be defined as a fraction of the maximum frequency: $w_o = \gamma w_{max}$. The ideal value for w_o was determined by applying various values for the fraction constant (γ) until the DDM results converged. After applying the Fourier filter, a cubic spline was used to obtain equal sized elements along the fracture trace. Figure 2 shows a comparison of the convergence results for the original and preprocessed fracture trace. Preprocessing the fracture trace led to convergent DDM results as indicated by the overlapping of the

fracture slip distribution curves for N and 2N number of elements. Furthermore, it can be observed that the preprocessing step preserved the overall shape of the fracture trace.

$$w = (u^2 + v^2)^{1/2} \tag{3}$$

$$H(u,v) = \frac{1}{1+\left[\frac{u^2+v^2}{w_o^2}\right]^2} \tag{4}$$

An example of a DDM surface elevation input map and the corresponding aperture and slip results is shown in Figure 3. The positive normal displacement is the aperture and the shear displacement is defined as the slip. It is important to note that the heterogeneous spatial distribution of the aperture and slip values within the fracture was solely due to the roughness of the fracture surface. To eliminate the edge effects, rectangular sections were obtained from the full fracture plane results. Flow simulations were then conducted on these rectangular fracture planes using the local cubic law model at steady state (Ishibashi et al., 2012). Local aperture values were converted to permeability using the cubic law (Witherspoon, 1980). A minimum local aperture of $1x10^{-10}m$ was defined for elements that did not open. Relevant flow pathways were defined as areas that have a flow rate value of at least one percent of the maximum flow rate. Based on the steady-state simulation results, the overall fracture hydraulic aperture and permeability were likewise calculated.

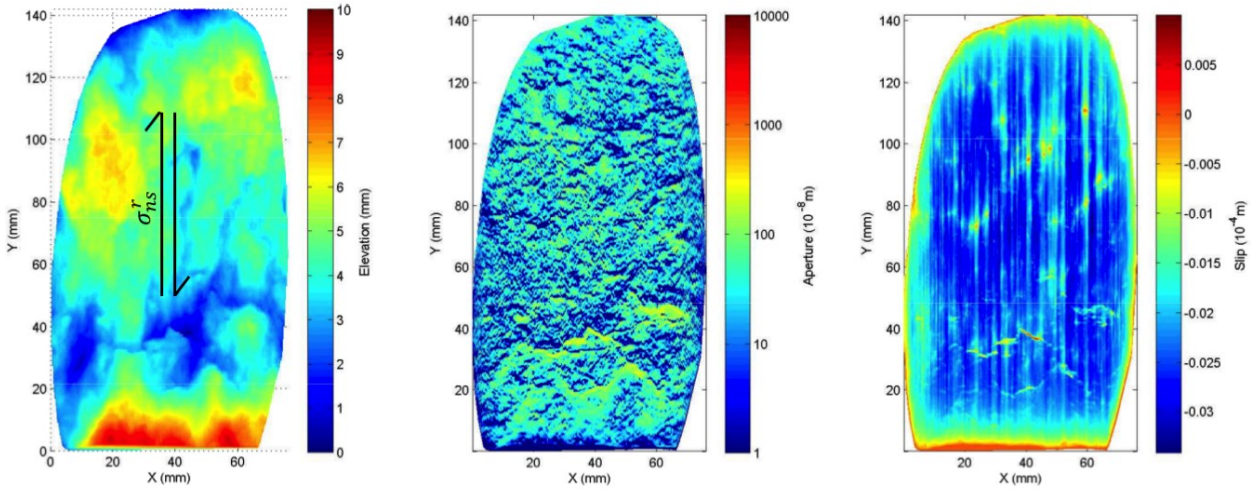

Figure 3: Sample DDM results for slip parallel to the longitudinal side of the fracture. The direction of the applied shear stress (σ_{ns}^r) is indicated by the arrows. The roughness of the fracture surface led to heterogeneous opening and slip distributions.

4. RESULTS

Various remote normal (σ_{nn}^r) and shear (σ_{ns}^r) stress values were applied on the fracture surface to observe the evolution of the aperture and slip distribution on the fracture plane. σ_{ns}^r was applied in two orientations with respect to the original fracture surface: longitudinal and lateral. Figure 4 and Figure 5 illustrate the aperture map evolution with respect to different σ_{nn}^r and σ_{ns}^r values for the longitudinal and lateral σ_{ns}^r directions, respectively. For all the simulated cases, there was no fluid present in the fracture during the stress application. Since there was no fluid in the fracture, the local opening of the fracture elements was exclusively due to the local stress interactions caused by the roughness of the fracture surface. As expected, increasing σ_{nn}^r reduced the fracture aperture values because of the increased resistance to slip. In addition, at $\sigma_{ns}^r = 6MPa$ and $\sigma_{nn}^r = 10MPa$, the results for both σ_{ns}^r orientations did not show a change in fracture aperture because the local slip values were too low. In contrast, increasing σ_{ns}^r increased the fracture aperture values because more elements opened with increased slip.

The changes in the spatial distribution of the fracture aperture have a significant effect on the flow connectivity behavior. To determine the fracture flow pattern evolution with stress, relevant normalized flow maps were analyzed. Figure 6 demonstrates the effect of increasing σ_{nn}^r at a constant σ_{ns}^r value. Higher flow conductivity was observed for lower σ_{nn}^r conditions. In addition, consistent flow channeling pathways emerged as the σ_{nn}^r increased. At the highest σ_{nn}^r case, the two dominant horizontal flow channeling pathways at the bottom of the fracture plane section can be observed. In contrast, increasing σ_{ns}^r had a positive effect on the fracture flow pattern evolution as shown in Figure 7. Having a higher σ_{ns}^r at constant σ_{nn}^r increased the likelihood of elements slipping at local stress conditions, which also increased the normal displacement. Similar to Figure 6, dominant flow pathways emerged as the flow was restricted, which occurred at lower σ_{ns}^r values. The observed dominant flow pathways can be traced back to the aperture evolution with stress.

In Figure 4 and Figure 5, it can be observed that, as σ_{ns}^r increases, there is increased formation of high aperture channels in the direction perpendicular to the σ_{ns}^r direction. These connected high aperture pathways have a profound effect in the permeability anisotropy orientations with respect to slip. Figure 8 illustrates the difference in flow connectivity patterns of different flow orientations. For the

same fracture aperture map, a pressure gradient was applied in two directions: perpendicular and parallel to the σ_{ns}^r direction. The results from the flow direction perpendicular to σ_{ns}^r (Figure 8b) exhibited a channelized flow pattern. Most of the flow paths for the perpendicular flow direction case occurred in the dominant flow channels. On the other hand, the results for the parallel flow direction (Figure 8c) showed a distributed flow pattern. These observations on the flow pattern behavior with respect to the flow and σ_{ns}^r directions were consistent with previous findings (Co and Horne, 2015).

Based on the steady-state flow simulations, the total fracture permeability was calculated for each stress condition and flow direction. Figure 9 shows the results for the longitudinal σ_{ns}^r direction while Figure 10 shows the results for the lateral σ_{ns}^r direction. The lowest permeability value was based on the default minimum local aperture for elements that remained closed after the application of stress. Consistent with trends observed in the aperture map evolution with stress, the fracture permeability was negatively correlated with σ_{nn}^r values due to the increased resistance to slip. Additionally, the fracture permeability was positively correlated with σ_{ns}^r values. There were a few observation points in Figure 10 that had a temporary decrease in permeability with an increase in σ_{ns}^r. This inconsistency was attributed to the small aperture values at high σ_{nn}^r values that led to inconsistent aperture patterns. This temporary decrease in fracture permeability was also observed in shear box flow experiments performed by Lee and Cho (2002). Overall, however, the fracture permeability increased with σ_{ns}^r for most of the simulated cases. Moreover, the general shape of the generated fracture permeability versus shear stress curves exhibited a higher rate of increase at smaller σ_{ns}^r values and a flattening at higher σ_{ns}^r values.

Furthermore, it was also observed that the permeability remained unchanged until the fracture slipped at the critical σ_{ns}^r value. The rough fracture surface created local stress interactions among the elements within the fracture, which increased the overall fracture resistance to slip. In addition to the effect of the applied stress conditions, the effect of the flow orientation was likewise considered. For both longitudinal and lateral σ_{ns}^r applications, the fracture permeability perpendicular to the σ_{ns}^r direction was consistently higher than the permeability parallel to σ_{ns}^r except for a few cases. The specific case runs in Figure 10 with a higher permeability for the parallel flow direction were at low σ_{ns}^r conditions relative to σ_{nn}^r, where the aperture values were small. Nevertheless, the overall trend of having a higher fracture permeability perpendicular to σ_{ns}^r in comparison to the permeability parallel to σ_{ns}^r concurred with the studies performed by Matsuki et al. (2006) and Nemoto et al. (2009).

As seen in Figure 3c, the roughness of the fracture surface created heterogeneous slip distributions within the fracture plane at different stress conditions. Thus, a single value is inadequate in describing the evolution of fracture slip due to stress application. In addition, it is difficult to determine the appropriate slip value to relate to the fracture permeability change. To determine the suitable representative fracture slip value, the overall distribution of the slip values within the fracture was investigated. Figure 11 demonstrates the variation of element slip values within the fracture. The arithmetic mean of the fracture slip values was chosen as the representative value because the fracture slip distributions were approximately normal in shape. The relationship between the mean absolute slip and the stress conditions for longitudinal and lateral σ_{ns}^r directions are shown in Figure 12 and Figure 13, respectively. The slip increased with σ_{ns}^r and decreased with σ_{nn}^r. Because the mean slip axis is in a logarithmic scale, cases with no slip were not plotted. Initial fracture slipping commenced when σ_{ns}^r was equal to or slightly above $0.6\sigma_{nn}^r$, which was expected since $\mu = 0.6$. The general shape of the mean slip behavior with σ_{ns}^r was consistent with the results for fracture permeability. In addition, unlike the fracture permeability, the mean slip behavior was consistent for all the simulated cases. This observation was due to the fact that fracture permeability measures aperture connectivity in space as opposed to individual slip values for each fracture element.

The fracture permeability relationship with slip was likewise investigated. Figure 14 and Figure 15 show the results for the longitudinal and lateral σ_{ns}^r directions, respectively. Near the critical σ_{ns}^r value ($\sigma_{ns}^r \cong 0.6\sigma_{nn}^r$), small slip values were calculated and no elements were opened. In addition, the overall shape of the permeability versus slip curves was consistent with experimental curves found in literature (Barton et al., 1985; Lee and Cho, 2002). Furthermore, the overall shape was also consistent with empirical models developed by Barton et al. (1985); Willis-Richards et al. (1996); and Dempsey et al. (2013). However, the key advantage of using the DDM model is that it provides a consistent physical framework to accurately model the changes in permeability and slip with stress. Contrastingly, the disadvantage of using empirical equations is that one set of parameters cannot consistently predict the permeability evolution with a wide range of stress conditions (Co and Horne, 2014). In addition, the DDM model simulates the aperture and slip distributions for the whole fracture plane instead of a single fracture trace. Simulating the two-dimensional spatial distribution of the aperture is crucial to predicting permeability anisotropy with respect to the applied σ_{ns}^r direction. In addition, imposing a uniform slip on the whole fracture surface to model shear stress application is not consistent with the heterogeneous slip distributions observed in this study. Another advantage of using the DDM model to investigate the permeability change with stress is that the impact of the surface roughness on the permeability evolution can be isolated. Because of the elastic deformation of the each element, the surface remains unchanged during stress application. Thus, a fundamental understanding of the effect of surface roughness on permeability evolution with stress can be developed. In contrast, inelastic effects such as breakage and gouge formation modify the fracture surface, which makes it difficult to ascertain the sources and mechanisms of permeability changes with stress.

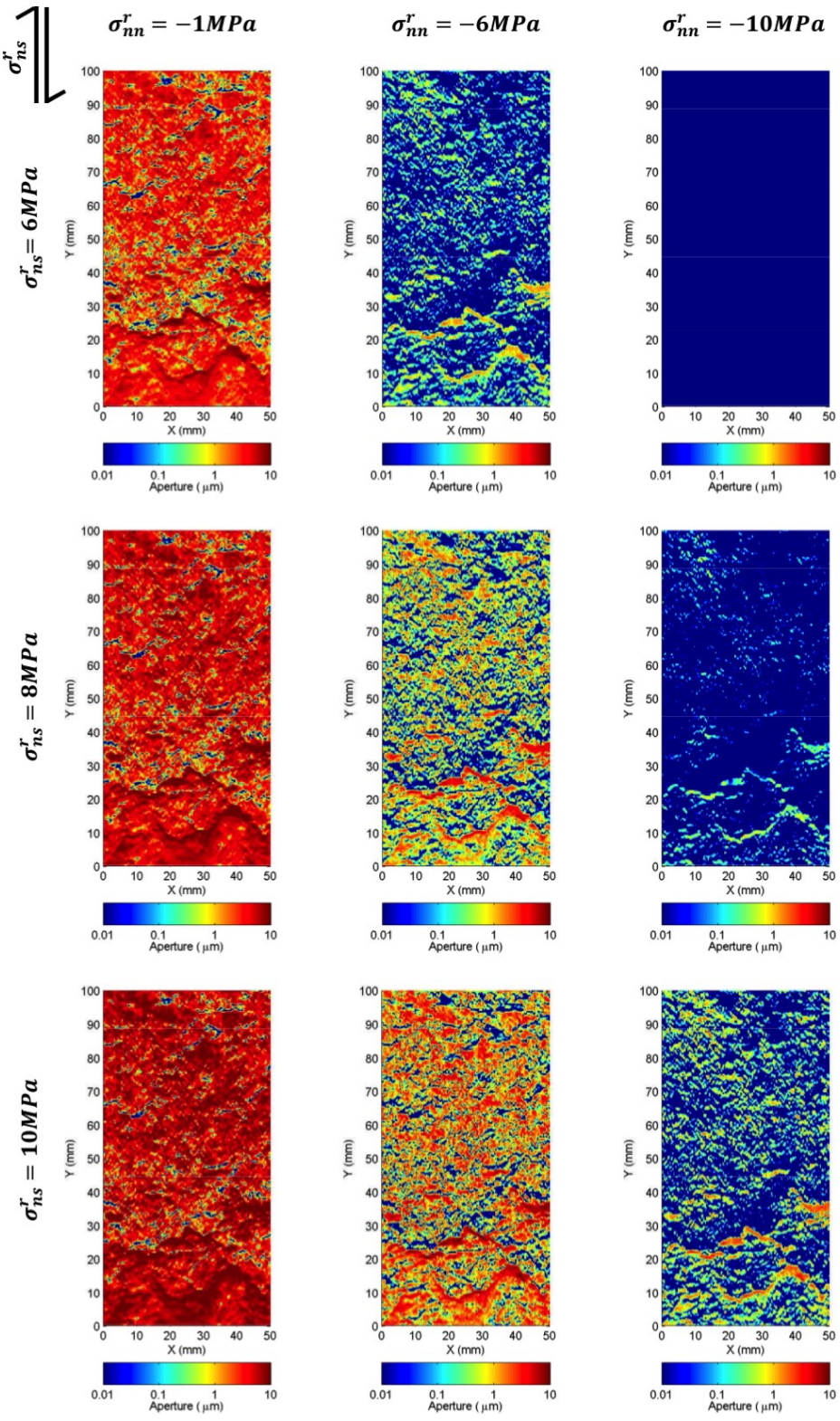

Figure 4: Aperture distribution for different normal (σ_{nn}^r) and shear (σ_{ns}^r) stress values calculated using the DDM model. The applied σ_{ns}^r was in the longitudinal direction.

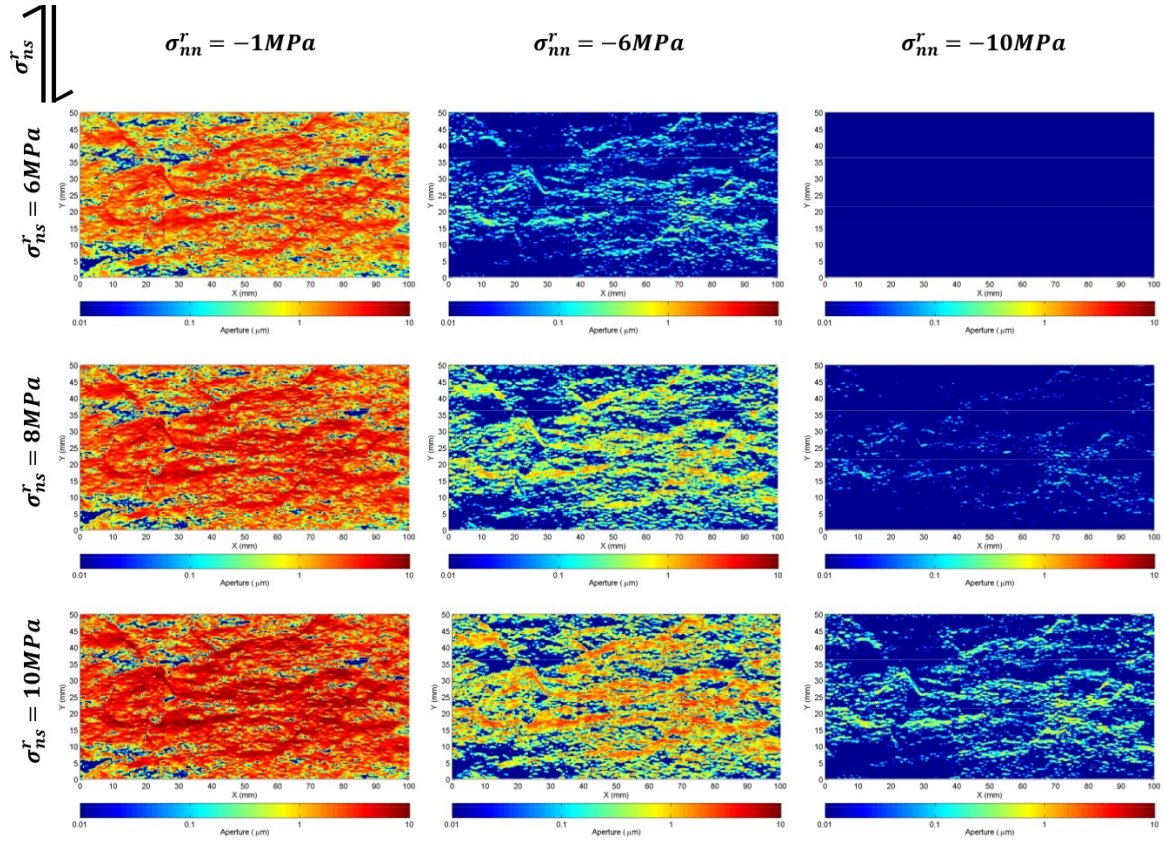

Figure 5: Aperture distribution for different normal (σ_{nn}^r) and shear (σ_{ns}^r) stress values calculated using the DDM model. The applied σ_{ns}^r was in the lateral direction.

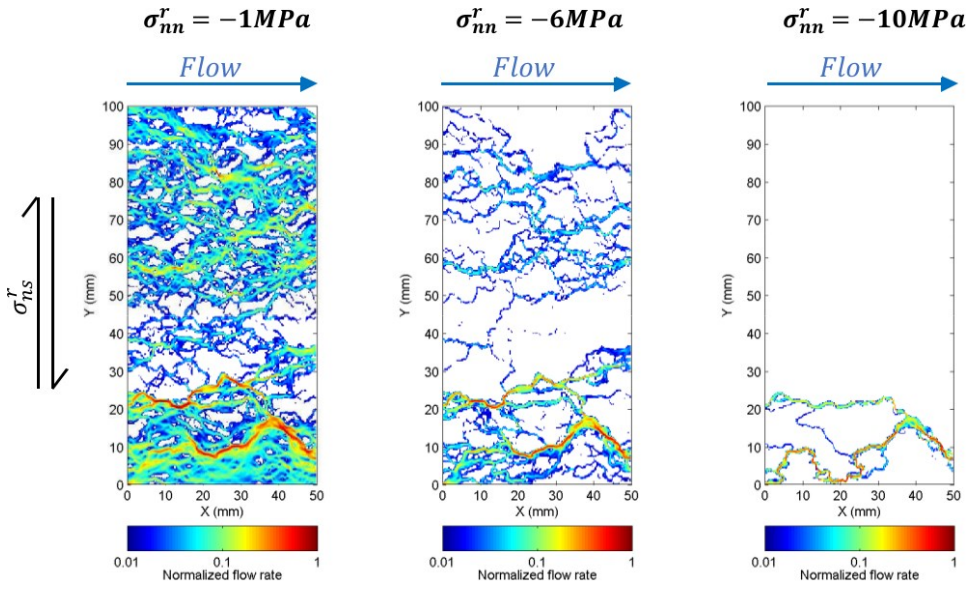

Figure 6: Effect of increasing the normal stress (σ_{nn}^r) on the flow connectivity patterns within the fracture at constant shear stress value ($\sigma_{ns}^r = 10MPa$). The applied σ_{ns}^r was in the longitudinal direction.

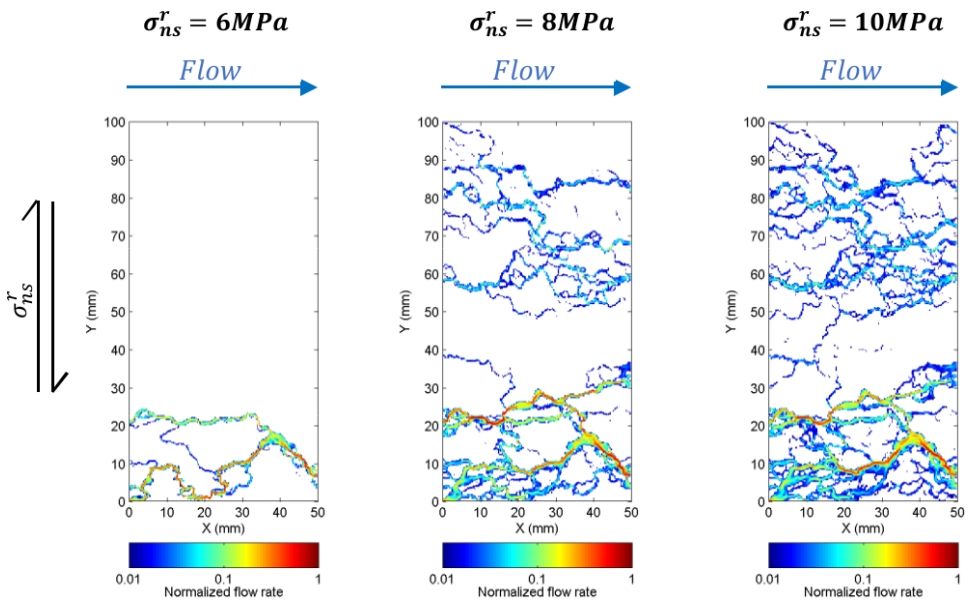

Figure 7: Effect of increasing the shear stress (σ_{ns}^r) on the flow connectivity patterns within the fracture at a constant normal stress value ($\sigma_{nn}^r = -6MPa$). The applied σ_{ns}^r was in the longitudinal direction.

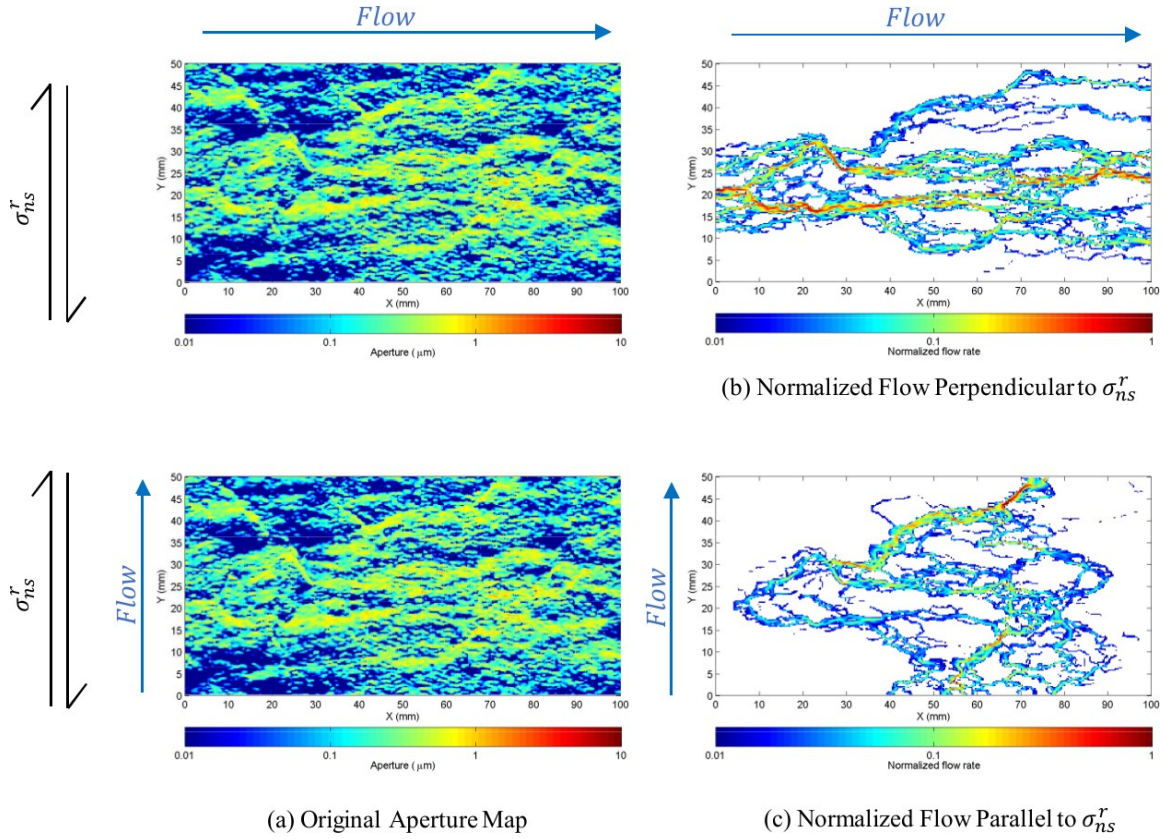

Figure 8: Comparison of flow connectivity patterns for different flow orientations with respect to the shear stress (σ_{ns}^r) direction ($\sigma_{nn}^r = -1MPa, \sigma_{ns}^r = 2MPa$). There was significant flow channeling in the direction perpendicular to the slip direction.

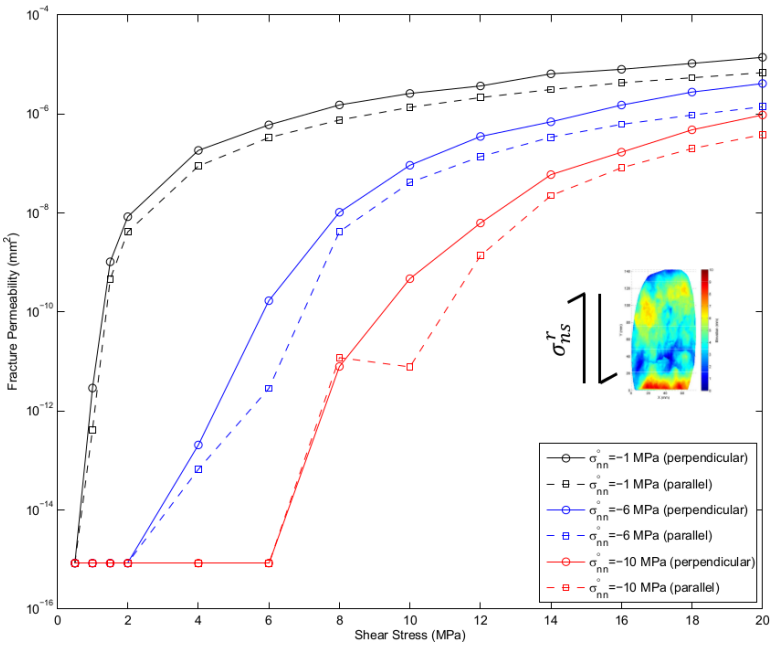

Figure 9: Fracture permeability results for different normal (σ_{nn}^r) and shear (σ_{ns}^r) stress conditions. The applied σ_{ns}^r was in the longitudinal direction.

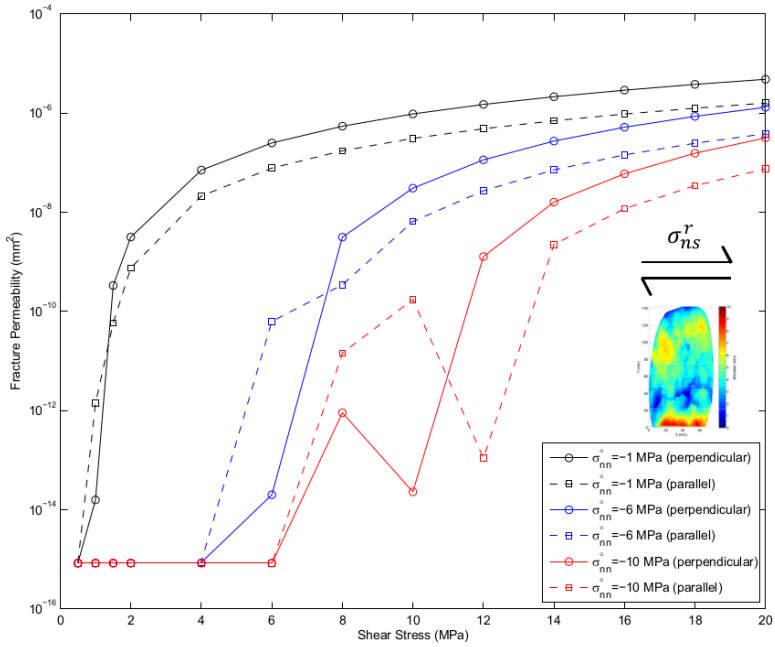

Figure 10: Fracture permeability results for different normal (σ_{nn}^r) and shear (σ_{ns}^r) stress conditions. The applied σ_{ns}^r was in the lateral direction.

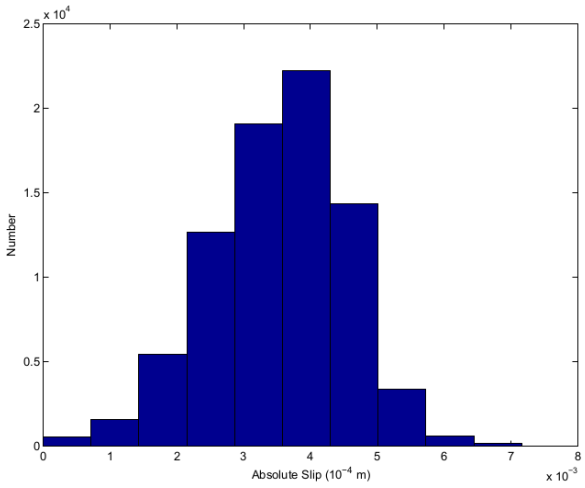

$\sigma_{nn}^{r} = -1MPa, \sigma_{ns}^{r} = 1MPa$

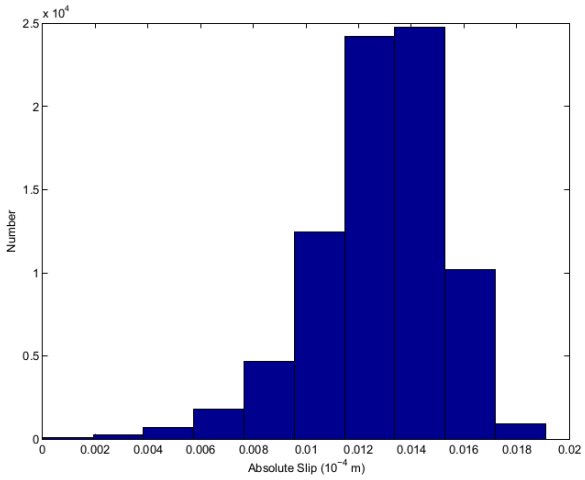

(b) $\sigma_{nn}^{r} = -1MPa, \sigma_{ns}^{r} = 1.5MPa$

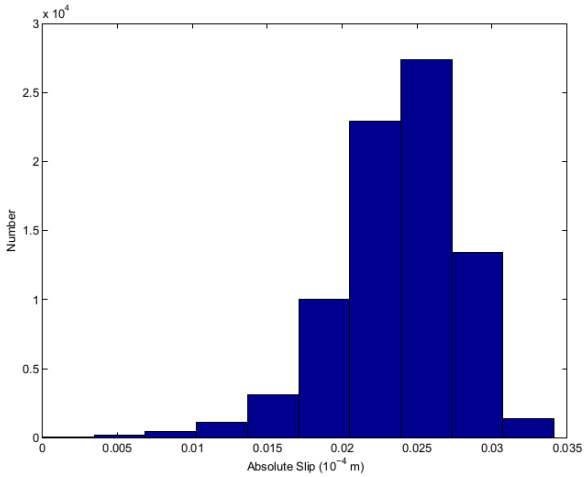

(c) $\sigma_{nn}^{r} = -1MPa, \sigma_{ns}^{r} = 2MPa$

Figure 11: Fracture slip distribution for different shear stress ($\boldsymbol{\sigma_{ns}^{r}}$) conditions ($\boldsymbol{\sigma_{nn}^{r} = -1MPa}$).

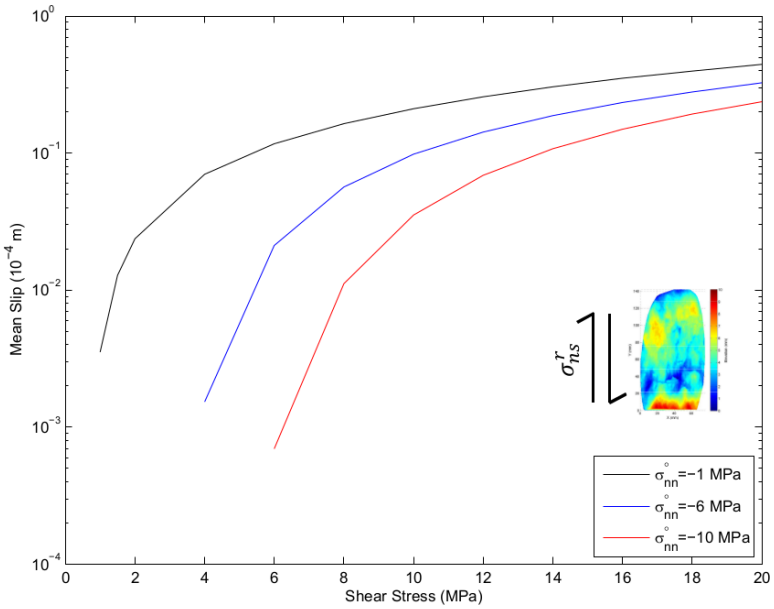

Figure 12: Mean fracture slip results for different normal (σ^r_{nn}) and shear (σ^r_{ns}) stress conditions. The applied σ^r_{ns} was in the longitudinal direction.

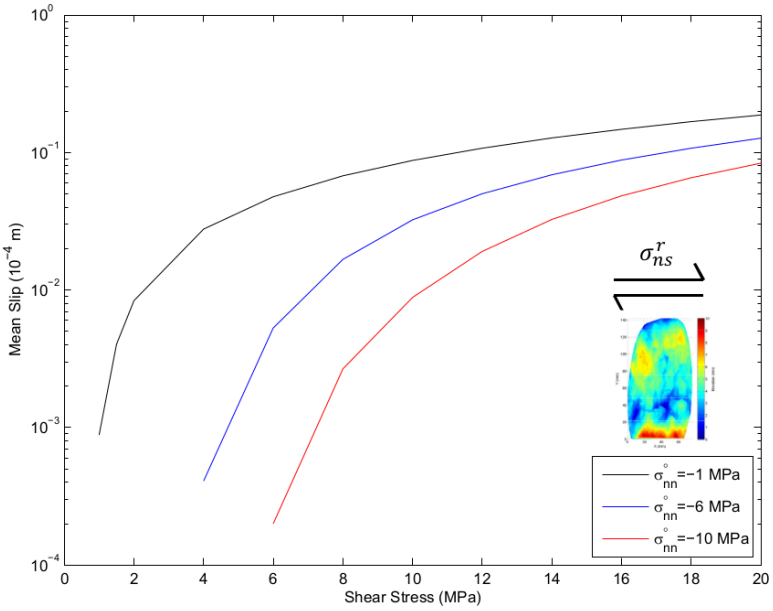

Figure 13: Mean fracture slip results for different normal (σ^r_{nn}) and shear (σ^r_{ns}) stress conditions. The applied σ^r_{ns} was in the lateral direction.

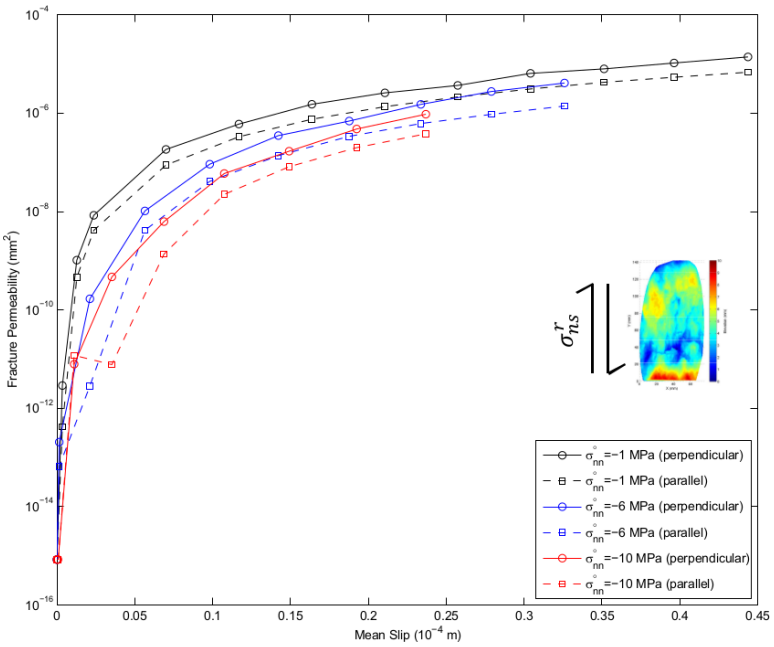

Figure 14: Fracture permeability versus mean slip at different normal stress (σ^r_{nn}) conditions. The applied σ^r_{ns} was in the longitudinal direction.

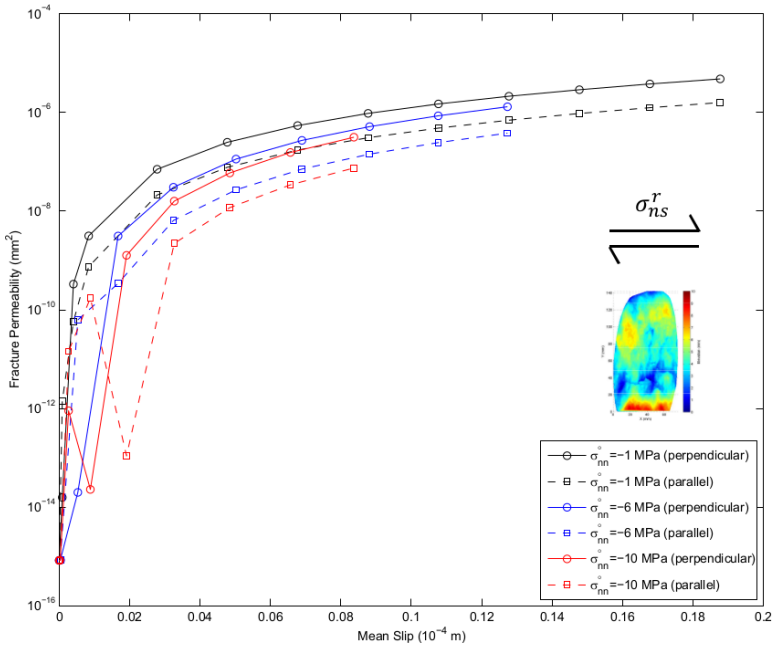

Figure 15: Fracture permeability versus mean slip at different normal stress (σ^r_{nn}) conditions. The applied σ^r_{ns} was in the lateral direction.

5. CONCLUSIONS AND RECOMMENDATIONS

For reservoirs found in tight rocks, such as shale gas and geothermal reservoirs, faults and fractures are the main conduits for flow. Thus, a fundamental understanding of the influence of fracture surface roughness on the fracture flow behavior is necessary for optimizing production in these systems. In addition, an accurate model of fracture permeability evolution with stress is essential for incorporating geomechanical effects in field scale simulations. Laboratory experiments in literature have demonstrated flow channeling effects due to fracture surface roughness.

In this study, the displacement discontinuity boundary element method with integrated complementarity (DDM) was used to investigate the changes in the spatial distribution of aperture and slip due to stress applied on a rough fracture surface. Shear stress was applied in the longitudinal and lateral directions with respect to the original fracture surface. In addition, steady-state flow simulations were conducted on the aperture maps generated from the DDM models to calculate the fracture permeability and evaluate the fracture flow behavior. Results exhibited heterogeneous aperture and slip distributions within the fracture plane for different stress conditions. In addition, fracture permeability and slip values were generated at various stress conditions. Both fracture permeability and slip increased with shear stress and decreased with normal stress. Moreover, the overall trend of the change in fracture permeability with slip was consistent with experimental results and empirical models found in literature. Higher rates of permeability changes were observed at lower shear stress and slip conditions. Another significant finding of this study was the permeability anisotropy with respect to the applied shear stress direction. The permeability was consistently higher in the direction perpendicular to the applied shear stress compared to the parallel direction. Moreover, channelized flow patterns were observed for the perpendicular flow direction while distributed flow patterns were observed in the parallel flow direction.

Because the DDM is a consistent physical model, it provides a comprehensive approach for understanding the fundamental effects of fracture roughness on the permeability and slip evolution of fractures under different stress conditions. In addition, flow patterns can be modeled and observed because this approach considers the spatial distribution of aperture in the fracture plane. For instance, a two-dimensional fracture aperture distribution is essential for modeling permeability anisotropy with respect to shear stress. For future work, a three-dimensional DDM (Kaven et al., 2012) application on rough fracture surfaces will be needed to account for the stress interactions between fracture traces and across fractures. In addition, the integration of inelastic effects on the local aperture development with the DDM model will create a broader understanding of the permeability evolution with stress.

ACKNOWLEDGEMENT

This research was supported by the grant of an Anne T. and Robert M. Bass Stanford Graduate Fellowship to the first author.

REFERENCES

Barton, N., Bandis, S., and Bakhtar, K.: Strength, Deformation and Conductivity Coupling of Rock Joints, International Journal of Rock Mechanics and Mining Sciences & Geomechanics Abstracts, 22, (1985), 121-140.

Co, C. and Horne, R.: Stress-Permeability Relationships in Low Permeability Systems: Application to Shear Fractures, Proceedings, 39th Stanford Geothermal Workshop, Stanford, CA (2015).

Co, C. and Horne, R.: Artificial Rough Fracture Generation using Sequential Gaussian Simulation (SGSIM): Correlating Spatial Aperture Characteristics to Flow Channeling Behavior, 2015 International Association for Mathematical Geosciences (IAMG) Conference, Freiberg, Germany, (2015).

Crouch, S.L., Starfield, A.M.: Boundary Element Methods in Solid Mechanics, Allen & Unwin, London, 1983.

Dempsey, D., Kelkar, S., Lewis, K., Hickman, S., Davatzes, N., Moos, D., and Zemach, E.: Modeling Shear Stimulation of the Desert Peak EGS Well 27-15 Using a Coupled Thermal-Hydrological-Mechanical Simulator, Proceedings, 47th US Rock Mechanics / Geomechanics Symposium, San Francisco, CA (2013).

Esaki, T., Du, S., Mitani, Y., Ikusada, K., and Jing, L.: Development of a Shear-Flow Test Apparatus and Determination of Coupled Properties for a Single Rock Joint. International Journal of Rock Mechanics and Mining Sciences, 36(5), (1999), 641-650.

Ishibashi, T., Watanabe, N., Hirano, N., Okamoto, A., and Tsuchiya, N.: Upgrading of Aperture Model based on Surface Geometry of Natural Fracture for Evaluating Channeling Flow, GRC Transactions, 36, (2012), 481-486.

Kaven, J. O., Hickman, S. H., Davatzes, N. C., and Mutlu, O.: Linear Complementarity Formulation for 3D Frictional Sliding Problems, Computational Geosciences, 16(3), (2012), 613-624.

Lee, H. and Cho, T.: Hydraulic Characteristics of Rough Fractures in Linear Flow under Normal and Shear Load, Rock Mechanics and Rock Engineering, 35(4), (2002), 299-318.

Matsuki, K., Y. Chida, K. Sakaguchi, and P. W. J. Glover (2006), Size effect on aperture and permeability of a fracture as estimated in large synthetic fractures, Int. J. Rock Mech. Min. Sci., 43, 726–755.

McClure, M. W. and Horne, R. N.: Investigation of Injection-Induced Seismicity Using a Coupled Fluid Flow and Rate/State Friction Model. Geophysics, 76(6), (2011), WC181-WC198.

Nemoto, K., N. Watanabe, N. Hirano, and N. Tsuchiya (2009), Direct Measurement of Contact Area and Stress Dependence of Anisotropic Flow through Rock Fracture with Heterogeneous Aperture Distribution, Earth Planet. Sci. Lett., 281, 81–87.

Pollard, D. D. and Fletcher, R. C.: Fundamentals of Structural Geology, Cambridge University Press, (2005).

Ritz, E., Mutlu, O., and Pollard, D. D.: Integrating Complementarity into the 2D Displacement Discontinuity Boundary Element Method to Model Faults and Fractures with Frictional Contact Properties, Computers & Geosciences, 45, (2012), 304-312.

Roberts, J., and T. D. Roberts (1978), Use of the Butterworth Low-Pass Filter for Oceanographic Data, J. Geophys. Res., 83(C11), 5510–5514, doi:10.1029/JC083iC11p05510.

Tester, J., Anderson, B. J., Batchelor, A. S., Blackwell, D. D., DiPippo, R., Drake, E. M., Garnish, J., Livesay, B., Moore, M. C., Nichols, K., et al.: The Future of Geothermal Energy, Massachusetts Institute of Technology, (2006).

Willis-Richards, J., Watanabe, K., and Takahashi, H.: Progress Toward a Stochastic Rock Mechanics Model of Engineered Geothermal Systems, Journal of Geophysical Research: Solid Earth, 101(B8), (1996), 17481-17496.

Witherspoon, P., Wang, J., Iwai, K., and Gale, J.: Validity of Cubic Law for Fluid Flow in a Deformable Rock Fracture, Water Resources Research, 16(6), (1980), 1016-1024.